# Superradiant instabilities of massive bosons around exotic compact objects

Lihang Zhou[1,2] Richard Brito[3] Zhan-Feng Mai[2,*] and Lijing Shao[2,4,†]

[1]*Department of Astronomy, School of Physics, Peking University, Beijing 100871, China*
[2]*Kavli Institute for Astronomy and Astrophysics, Peking University, Beijing 100871, China*
[3]*CENTRA, Departamento de Física, Instituto Superior Técnico—IST, Universidade de Lisboa—UL,*
*Avenida Rovisco Pais 1, 1049 Lisboa, Portugal*
[4]*National Astronomical Observatories, Chinese Academy of Sciences, Beijing 100012, China*

Superradiantly unstable ultralight particles around a classical rotating black hole (BH) can form an exponentially growing bosonic cloud, which have been shown to provide an astrophysical probe to detect ultralight particles and constrain their mass. However, the classical BH picture has been questioned, and different theoretical alternatives have been proposed. Exotic compact objects (ECOs) are horizonless alternatives to BHs featuring a reflective surface (with a reflectivity $\mathcal{K}$) in place of the event horizon. In this work, we study superradiant instabilities around ECOs, particularly focusing on the influence of the boundary reflection. We calculate the growth rate of superradiant instabilities around ECOs and show that the result can be related to the BH case by a correction factor $g_{\mathcal{K}}$, for which we find an explicit analytical expression and a clear physical interpretation. Additionally, we consider the time evolution of superradiant instabilities and find that the boundary reflection can either shorten or prolong the growth timescale. As a result, the boundary reflection alters the superradiance exclusion region on the Regge plane, potentially affecting constraints on the mass of ultralight particles. For a mildly reflective surface ($|\mathcal{K}| \lesssim 0.5$), the exclusion region is not substantially changed, while significant effects from the boundary reflection can occur for an extreme reflectivity ($|\mathcal{K}| \gtrsim 0.9$).

## I. INTRODUCTION

Ultralight bosons have been proposed by different theories as elementary particles beyond the Standard Model of particle physics. Examples include (i) the QCD axion, introduced to solve the strong charge-parity problem [1–3], (ii) a plenitude of axionlike particles (ALPs), predicted by the string theory and called an "axiverse" [4,5], and (iii) dark photons [6]. These ultralight bosons, which would naturally couple weakly to baryonic matter, have been shown to be promising dark matter candidates [7–9].

In addition to some ground-based experiments (see, e.g., Refs. [9,10]), astrophysical environments, such as the vicinity of black holes (BHs), also provide natural test beds for detecting ultralight particles. This relies on a mechanism called BH superradiance (for a comprehensive review, see Ref. [11]). Consider a field of ultralight particles with mass $\mu$, located near a rotating BH. When the Compton wavelength of the particle is comparable to the horizon radius of the BH, the particle field can form quasibound states around the BH and extract energy and angular momentum effectively from the BH if the following superradiance condition is satisfied:

$$\omega_R < \frac{ma}{2Mr_+}, \tag{1}$$

where $\omega_R$ is the real part of the frequency of the massive field, which is typically close to the mass $\mu$ of the ultralight particle; $m$ is the magnetic quantum number; and $a, M, r_+$ are the spin, mass, and horizon radius of the BH, respectively. An intuitive understanding of this condition is that superradiance occurs whenever the angular velocity of the field, $\omega_R/m$, is less than that of the spacetime $a/2Mr_+$. When the superradiance condition is met, the bosonic field can turn unstable as more and more particles are produced from the extracted energy and angular momentum. These particles remain bounded to the BH by gravity and form an exponentially growing bosonic cloud. This phenomenon is the so-called superradiant instability. Superradiant instabilities of BHs have been thoroughly studied using perturbation theory but also numerical relativity, with studies including the computation of the unstable eigenfrequencies [12–23], linear and nonlinear time evolutions of the instability [24–27], the understanding of nonlinear effects such as the "bosenova" or scalar emission

---

*Corresponding author: zhanfeng.mai@gmail.com
†Corresponding author: lshao@pku.edu.cn

induced by self-interactions [28–31], and the computation of gravitational wave (GW) emission by the bosonic cloud [26,32–38]. In particular, it has been shown that superradiant instabilities can spin down rotating BHs and leave exclusion regions on the BH spin-mass plane (Regge plane). Since these regions are related to the mass of ultralight particles, they can be used to constrain the latter through the measurement of the spin and mass of astrophysical BHs [5,26,33,39,40].

In this paper, we shall not restrict our discussion to BHs. Classical BHs, namely, Kerr BHs, as a solution of Einstein's general relativity (GR), have singularities at $r = 0$, which are hidden within event horizons. However, this classical BH picture leads to puzzles [41], for example, the information paradox of evaporating BHs [42,43]. In different contexts, including some quantum gravity candidates, exotic compact objects (ECOs) as horizonless alternatives to classical BHs, have been proposed and studied. Examples include fuzzballs in string theory [44,45], boson stars and oscillations [46], gravitational condensate stars, i.e., gravastars [47] and wormholes [48,49]. A more comprehensive list of proposed ECOs can be found in Refs. [41,50].

ECOs have also been dubbed as "BH mimickers" [51]. They have no event horizon, and their surfaces are reflective, in contrast with the BH event horizon which only allows particles and waves to fall inwards. In a simple phenomenological model, widely used in the literature, one can assume the presence of a boundary at $r_0 \gtrsim r_+$, with a reflectivity $\mathcal{K}$, while the external spacetime is still described by the usual Kerr geometry. The modified inner boundary condition may result in colorful phenomenology, including modified quasinormal modes (QNMs) [52–55], ergoregion instabilities [52,54–57], and GW "echo" signals [41,50,58,59], to name a few examples. Although there is no definite proof of the existence of BH horizons [52], the advent of GW detection and the improvements in its precision may provide a unique opportunity to probe physics at the near-horizon scale and constrain to very high precision the existence of a reflecting surface (see Refs. [41,60] for recent reviews).

Recently, superradiant instabilities of ultralight particles around ECOs, have also been studied by Guo et al. [61,62]. In particular, a first effort was made in Ref. [61] in investigating massive scalar perturbations with a modified boundary condition, using a purely analytic approach in the nonrelativistic regime, where $\alpha \equiv \mu M \ll 1$, where again $\mu$ and $M$ are the masses of the bosonic field and the BH, respectively. The goal of this paper is to study this subject in more detail and, for the first time, explicitly show how the boundary reflection influences the growth of massive scalar perturbations around ECOs.

This paper is organized as follows. In Sec. II, we derive the equations of motion for massive scalar perturbations and specify the boundary conditions. At the end of that section, a discussion can be found regarding the difference in the boundary conditions set by Guo et al. [61] and by us. In Sec. III we solve the eigenvalue problem. We first introduce our analytic method, from which we obtain our key result, the correction factor $g_{\mathcal{K}}$ [see Eq. (36) below]. We also calculate the eigenfrequencies using a semianalytic method and a continued fraction method, followed by a comparison between different methods. The physical meaning of the correction factor $g_{\mathcal{K}}$ is investigated in Sec. IV by making use of the energy-momentum conservation. Section V is devoted to a discussion on the time evolution of superradiant instabilities around ECOs, with a particular focus on the influence of the boundary reflection. Section VI discusses the implications of the possible boundary reflection for the constraints on the ultralight particle mass. Our summary and conclusion can be found in Sec. VII. In this work, we use the $(-, +, +, +)$ convention and set $G = c = \hbar = 1$.

## II. BOSONIC CLOUD AROUND AN ECO

We consider massive scalar perturbations in the following spacetime background: we assume that the geometry outside of the ECO is described by the Kerr metric, with the line element in Boyer-Lindquist coordinates,

$$ds^2 = -\left(1 - \frac{2Mr}{\rho^2}\right)dt^2 + \frac{\rho^2}{\Delta}dr^2 - \frac{4Mr}{\rho^2}a\sin^2\theta d\phi dt$$
$$+ \rho^2 d\theta^2 + \left[(r^2 + a^2)\sin^2\theta + \frac{2Mr}{\rho^2}a^2\sin^4\theta\right]d\phi^2,$$

$$(2)$$

where $a = J/M$ is the spin angular momentum normalized by the mass of the ECO, $\rho^2 \equiv r^2 + a^2\cos^2\theta$, and $\Delta \equiv r^2 - 2Mr + a^2$. For a Kerr BH, the event horizon and the Cauchy horizon are located at $r_+ = M + \sqrt{M^2 - a^2}$ and $r_- = M - \sqrt{M^2 - a^2}$, respectively; $r_+$ is normally taken to be the inner boundary in the study of superradiant instabilities, with a purely ingoing boundary condition [13,17,21]. However, for an ECO, we replace the event horizon with a reflective surface located at $r_0 = r_+(1 + \epsilon)$, where $\epsilon \ll 1$. This surface reflects a portion of the ingoing wave, parametrized by the reflectivity $\mathcal{K}$.

In a curved spacetime, a test scalar field with mass $\mu$ satisfies the Klein-Gordon equation,

$$(\nabla^\nu \nabla_\nu - \mu^2)\Psi = 0. \qquad (3)$$

To study characteristic modes of the perturbation field, we separate variables as follows:

$$\Psi(t, r, \theta, \phi) = e^{-i\omega t}e^{im\phi}R_{lm}(r)S_{lm}(\theta), \qquad (4)$$

where $\omega \in \mathbb{C}$ is the complex eigenfrequency, and the integers $l \geq 0, m \in [-l, l]$ are the angular and magnetic quantum numbers, respectively. Expanding the Klein-Gordon equation in a Kerr metric background, we obtain the following equations of motion:

$$\frac{\mathrm{d}}{\mathrm{d}r}\left(\Delta \frac{\mathrm{d}R_{lm}}{\mathrm{d}r}\right) + \left[\frac{\omega^2(r^2 + a^2)^2 - 4Mam\omega r + m^2 a^2}{\Delta} - (\omega^2 a^2 + \mu^2 r^2 + \Lambda_{lm})\right] R_{lm}(r) = 0, \tag{5}$$

$$\frac{1}{\sin\theta} \frac{\mathrm{d}}{\mathrm{d}\theta}\left(\sin\theta \frac{\mathrm{d}S_{lm}}{\mathrm{d}\theta}\right) + \left[a^2(\omega^2 - \mu^2)\cos^2\theta - \frac{m^2}{\sin^2\theta} + \Lambda_{lm}\right] S_{lm}(\theta) = 0, \tag{6}$$

where $\omega$ and $\Lambda_{lm}$ are the eigenvalues to be solved. The eigenfunctions $S_{lm}$ of Eq. (6) are a series of spin-weighted spheroidal harmonics labeled by $l$ and $m$, with the eigenvalues $\Lambda_{lm} = l(l+1) + \mathcal{O}[a^2(\mu^2 - \omega^2)]$; see Ref. [63] for an analytical expansion of $\Lambda_{lm}$ in terms of $a\sqrt{\mu^2 - \omega^2}$. Here, we introduce a complex number $l'$ to denote $\Lambda_{lm}$ as

$$\Lambda_{lm} = l'(l' + 1). \tag{7}$$

When $\omega \approx \mu$ and $\alpha = \mu M \ll 1$ are satisfied, $l'$ is very close to the augular quantum number $l$. Therefore, in Eq. (5), $\Lambda_{lm}$ can be treated as a known number and only the eigenfrequency $\omega$ needs to be found.

In order to find $\omega$ from Eq. (5), we also need to impose appropriate boundary conditions. When $r \to \infty$, we take the decaying solution of $R_{lm}$ [17],

$$\lim_{r \to \infty} R_{lm}(r) \sim r^{-1 + (2\omega^2 - \mu^2)M/\kappa} \mathrm{e}^{-\kappa r}, \tag{8}$$

where

$$\kappa = \sqrt{\mu^2 - \omega^2}, \qquad \mathrm{Re}\,\kappa > 0. \tag{9}$$

When investigating the behavior of $R_{lm}$ near the inner boundary $r_0$, it is useful to introduce the tortoise coordinate,

$$r^* = \int \frac{r^2 + a^2}{\Delta} \mathrm{d}r$$
$$= r + \frac{2Mr_+}{r_+ - r_-} \ln|r - r_+| - \frac{2Mr_-}{r_+ - r_-} \ln|r - r_-|, \tag{10}$$

and define

$$Y = (r^2 + a^2)^{1/2} R_{lm}(r). \tag{11}$$

The location of the boundary can be expressed in the tortoise coordinate, $r_0^* = r^*(r_0)$. Then the radial equation (5) can be rewritten in the standard form of a wave equation $\mathrm{d}^2 Y/\mathrm{d}r^{*2} + VY = 0$, where the effective potential reads

$$V(r) = -\frac{\Delta(2Mr^3 + a^2 r^2 - 4Ma^2 r + a^4)}{(r^2 + a^2)^4}$$
$$\quad - \frac{\Delta(\mu^2 r^2 + a^2 \omega^2 - 2ma\omega + \Lambda_{lm})}{(r^2 + a^2)^2} + \left(\omega - \frac{ma}{r^2 + a^2}\right)^2. \tag{12}$$

Since $r_0 \approx r_+$, when $r \to r_0$ we have $\Delta \approx 0$, and therefore, in this limit, the two independent solutions of $Y$ are $\mathrm{e}^{\pm\mathrm{i}(\omega - \omega_c)\Delta r^*}$, where $\Delta r^* = r^* - r_0^*$, and

$$\omega_c = \frac{ma}{r_+^2 + a^2}. \tag{13}$$

For an ECO, the wave function near $r_0$ should be a superposition of ingoing and outgoing waves [64],

$$\lim_{\Delta r_* \to 0} Y \sim \mathrm{e}^{-\mathrm{i}(\omega - \omega_c)\Delta r^*} + \mathcal{K}\mathrm{e}^{\mathrm{i}(\omega - \omega_c)\Delta r^*}, \tag{14}$$

where $\mathcal{K}$ is the boundary reflectivity; $|\mathcal{K}|$ denotes the proportion of the incident wave reflected at $r_0$, and $\arg(\mathcal{K})$ is the phase shift.

Note that the inner boundary condition (14) in our treatment differs from Eq. (27) in Ref. [61]. In the latter, they wrote $\mathrm{e}^{-\mathrm{i}(\omega - \omega_c)r^*} + \mathcal{R}(\omega)\mathrm{e}^{\mathrm{i}(\omega - \omega_c)r^*}$ and the location $r_0^*$ of the reflective surface is not explicitly specified. Their definition is related to ours by $\mathcal{R}(\omega) = \mathcal{K}\mathrm{e}^{-2\mathrm{i}(\omega - \omega_c)r_0^*}$. With our definition, the physical meaning of the reflectivity $\mathcal{K}$ is clearer. At the reflective boundary, we have $\Delta r^* = 0$, and the amplitudes of the ingoing and outgoing waves at the reflective boundary are 1 and $\mathcal{K}$, respectively, up to a common constant. This means that $|\mathcal{K}|$ is simply the reflected proportion, and $|\mathcal{K}| = 1$ represents a "perfect reflection," up to a phase shift if $\mathcal{K}$ is complex.

Finally, the radial equation (5), together with Eqs. (8) and (14), defines an eigenvalue problem. This will be solved in the following where we will compute the complex eigenfrequencies $\omega = \omega_R + \mathrm{i}\omega_I$, where the real part $\omega_R$ denotes the energy level of the bosonic cloud and the imaginary part $\omega_I$ represents the growth rate of the superradiant instability.

## III. GROWTH RATE OF SUPERRADIANT INSTABILITY

### A. Analytic method

In the "nonrelativistic" regime $\alpha = \mu M \ll 1$, we have $\omega \approx \mu$ and can solve Eq. (5) using matched asymptotic expansions. This approach, found by Detweiler [13], has been used to study superradiant instabilities around BHs [14,18,21,22] and was recently extended by Guo *et al.* [61] to account for a boundary reflection. Here, we further develop it with an ECO boundary condition. This can be done by solving the radial equation in the "far" and "near" regions, respectively, and matching the two solutions in the "overlap" region.

In the far region where $r \gg M$, to leading order in $\alpha$, Eq. (5) can be written as

$$\frac{d^2(rR)}{dr^2} + \left[ (\omega^2 - \mu^2) + \frac{2M\mu^2}{r} - \frac{l'(l'+1)}{r^2} \right](rR) = 0, \quad (15)$$

where we have dropped subscripts $(l, m)$ for notation simplicity. Following Detweiler [13], we define

$$\nu = M\mu^2/\kappa, \quad (16)$$

where $\kappa$ was defined in Eq. (9). Then the solution to Eq. (15) with the decaying boundary condition at infinity reads

$$R_{\text{far}}(r) = (2\kappa r)^{l'} e^{-\kappa r} U(l'+1-\nu, 2l'+2; 2\kappa r), \quad (17)$$

where $U(a, b, c; x)$ is the Tricomi confluent hypergeometric function with respect to $x$. If $l'+1-\nu = -n$ is an integer, $U(a, b, c; x)$ reduces to a polynomial, which, in quantum mechanics, corresponds to eigenstates of hydrogen atoms, with $n = 0, 1, 2\ldots$ being the radial quantum number. However, since the inner boundary condition is different from that of hydrogen atoms, we must introduce a small deviation $\delta\nu \in \mathbb{C}$, via

$$\nu = l' + n + 1 + \delta\nu, \quad (18)$$

and the eigenfrequency is

$$\omega = \mu\sqrt{1 - \frac{\alpha^2}{\nu^2}} = \omega_R + i\omega_I. \quad (19)$$

The latter equation is derived from the definition of $\nu$ in Eq. (16) directly.

We now explore the solution of $R(r)$ in the near region $r \sim r_0$. Here, we introduce a dimensionless distance,

$$z \equiv \frac{r - r_+}{r_+ - r_-}, \quad (20)$$

and the location of the inner boundary is

$$z_0 \equiv \frac{r_0 - r_+}{r_+ - r_-}. \quad (21)$$

Then, to leading order in $\alpha$, Eq. (5) can be written as

$$z(z+1)\frac{d}{dz}\left[z(z+1)\frac{dR}{dz}\right] + V(z)R = 0, \quad (22)$$

where[1]

$$V(z) = p^2 - l'(l'+1)z(z+1), \quad (23)$$

$$p = \frac{2Mr_+(\omega - \omega_c)}{r_+ - r_-}, \quad (24)$$

and $\omega_c$ is defined in Eq. (13). The solution is

$$R_{\text{near}}(z) = \left(\frac{z}{z+1}\right)^{-ip} G(-l', l'+1; 1+2ip; z+1), \quad (25)$$

where $G(a, b; c; x)$ is any solution to the hypergeometric equation with respect to $x$. There are two independent solutions [65],[2]

$$u_3 = (-z)^{l'} {}_2F_1(-l', -l'+2ip; -2l'; -z^{-1}),$$
$$u_4 = (-z)^{-l'-1} {}_2F_1(l'+1, l'+1+2ip; 2l'+2; -z^{-1}), \quad (26)$$

where ${}_2F_1$ is the hypergeometric function. With these two solutions, $R_{\text{near}}$ can be written as

$$R_{\text{near}} = \left(\frac{z}{1+z}\right)^{-ip}(b_3 u_3 + b_4 u_4). \quad (27)$$

The ratio of the coefficients $b_3$, $b_4$ is determined by the inner boundary condition (14). Details are provided in the Appendix, and the result is

---

[1]Our definition of $p$ differs from $P$ in Detweiler [13] by a minus sign.

[2]In Ref. [13], the term corresponding to $2l'+2$ is incorrectly written as $2l+1$.

$$\frac{b_4}{b_3} = -\frac{\Gamma(-2l')\Gamma(l'+1)}{\Gamma(-l')\Gamma(2l'+2)} \frac{\mathcal{K}z_0^{-2ip}\Gamma(2ip+1)\Gamma(l'-2ip+1) - \Gamma(1-2ip)\Gamma(l'+2ip+1)}{\mathcal{K}z_0^{-2ip}\Gamma(2ip+1)\Gamma(-l'-2ip) - \Gamma(1-2ip)\Gamma(2ip-l')}. \tag{28}$$

Let us note that, to obtain Eq. (22), besides $\alpha \ll 1$, we have implicitly assumed two additional conditions by neglecting terms at higher orders in $\alpha$,[3] namely,

$$\alpha^2(1-\omega_c/\omega) \ll l(l+1)\sqrt{1-a^2/M^2}, \tag{29}$$

$$z \ll \min(l^2/\alpha^2, l/\alpha). \tag{30}$$

The former condition may not be satisfied even for $\alpha \ll 1$ if the spin is extreme $a/M \sim 1$, requiring the inclusion of the next-to-leading order correction for highly spinning BHs [22]. Here, we do not include this correction for simplicity. The latter condition gives the regime of validity of the near region solution (27).

The far region with $r \gg M$ and the near region with $z \ll \min(l^2/\alpha^2, l/\alpha)$ have an overlap when $\alpha$ is small enough, and thus, the two solutions can be matched.

First, one can expand the far region solution in the small-$r$ limit, keeping only dominant terms,

$$R_{\text{far}}(r) = (-1)^n \frac{\Gamma(2l'+2+n)}{\Gamma(2l'+2)}(2\kappa r)^{l'}$$
$$+ (-1)^{n+1}\delta\nu\Gamma(2l'+1)\Gamma(n+1)(2\kappa r)^{-l'-1}, \tag{31}$$

where $\kappa r \ll 1$ and $|\delta\nu| \ll 1$. Also, the large-$r$ limit of the near region solution is

$$R_{\text{near}}(r) = b_3\left(\frac{-r}{r_+-r_-}\right)^{l'} + b_4\left(\frac{-r}{r_+-r_-}\right)^{-l'-1}. \tag{32}$$

The two expansions should be linearly dependent, which determines $\delta\nu$ and $\omega$.

When doing the calculation, we make use of the fact that $l' \approx l$ so only $l$ appears in the final results. However, the factor $\Gamma(-2l')/\Gamma(-l')$ needs to be treated with care. As in Ref. [22], we take the limit $l' \to l$, and it becomes

$$\lim_{l'\to l}\frac{\Gamma(-2l')}{\Gamma(-l')} = \lim_{\epsilon\to 0}\frac{\Gamma(-2l-2\epsilon)}{\Gamma(-l-\epsilon)} = \frac{(-1)^l}{2}\frac{\Gamma(l+1)}{\Gamma(2l+1)}. \tag{33}$$

We also take into account that $|\delta\nu| \ll 1$, which allows us to obtain $\omega$ with a Taylor expansion. Finally, we obtain

$$M\omega_R = \alpha\left[1 - \frac{\alpha^2}{2(l+n+1)^2}\right], \tag{34}$$

$$M\omega_I = g_{\mathcal{K}}\alpha^{4l+5}\left(\frac{ma}{2M} - \omega_R r_+\right)\frac{2^{4l+2}(2l+n+1)!}{(l+n+1)^{2l+4}n!}\left[\frac{l!}{(2l+1)!(2l)!}\right]^2\prod_{j=1}^l\left[j^2\left(1-\frac{a^2}{M^2}\right) + \left(2r_+\omega_R - \frac{ma}{M}\right)^2\right], \tag{35}$$

where we have defined

$$g_{\mathcal{K}} = \frac{1 - |\mathcal{K}|^2}{1 + |\mathcal{K}|^2 + 2\,\text{Re}(A^2z_0^{-2ip}\mathcal{K})/|A|^2}, \tag{36}$$

where $A \equiv \prod_{j=1}^l(j-2ip)$ with $p$ defined in Eq. (24).

Equation (36) is our key result. The most important feature of our analytic result is that the growth rate $M\omega_I$ when including a (partially) reflective boundary condition differs from that of the BH case only by the factor $g_{\mathcal{K}}$. This factor does not alter the superradiance condition (1), namely that when $\omega_R < ma/2Mr_+$, the scalar field extracts energy and angular momentum from the ECO, growing exponentially.

When $\mathcal{K} = 0$, we have $g_{\mathcal{K}} = 1$, and the growth rate recovers the BH case, which was found by Detweiler [13] (except for a $1/2$ factor[4]) and other studies (see, e.g., Ref. [21]). The factor $g_{\mathcal{K}}$ hence represents the correction introduced by the boundary reflection. The denominator of this factor can be written as

$$1 + |\mathcal{K}|^2 + 2|\mathcal{K}|\cos\varphi, \tag{37}$$

where $\varphi \equiv 2\sum_{j=1}^l \arctan(-2p/j) - 2p\ln z_0 + \arg\mathcal{K}$. When $p$ changes, the denominator oscillates between $(1-|\mathcal{K}|)^2$ and $(1+|\mathcal{K}|)^2$. Therefore, we have

---

[3]These two conditions are found by comparing the dominant term $p^2 - \Lambda_{lm}z(z+1)$ with subdorminant terms at $\mathcal{O}(\alpha^2)$ in the full suppression of $V(z)$, which was given in Ref. [22].

[4]Our result (35), when $g_{\mathcal{K}} = 1$, turns out to be the half of the growth rate obtained in Ref. [13]. This could be explained by a missing $1/2$ factor that should have been on the right-hand side of Eq. (23) in Ref. [13], possibly stemming from an inappropriate treatment of $\Gamma(-2l')/\Gamma(-l')$. This $1/2$ factor is also discussed in Refs. [18,22]. As a comparison, our result agrees with Eq. (2.32) of Ref. [21].

$$\frac{1 - |\mathcal{K}|}{1 + |\mathcal{K}|} \leq g_{\mathcal{K}} \leq \frac{1 + |\mathcal{K}|}{1 - |\mathcal{K}|}. \qquad (38)$$

The value of $z_0$ will influence the (quasi)period of the oscillation. For example, when $z_0$ is small enough so that $-2p \ln z_0$ is the dominant term in $\varphi$, the change in $p$ that accounts for a full oscillation cycle is $\sim \pi / |\ln z_0|$. In this paper, we will illustrate results obtained with $z_0 = 10^{-5}$, and smaller values of $z_0$ will result in denser oscillatory patterns.

The physical meaning of $g_{\mathcal{K}}$ will be discussed in Sec. IV.

## B. Semianalytic method

The above method can yield an analytic result and clearly show how the boundary reflection changes the growth rate. However, to get more accurate results, the following semi-analytic method may be adopted, which was also used in Ref. [5] and similar to the method used in Ref. [66]. In the matching procedure presented above, only terms proportional to $r^{l'}$ and $r^{-l'-1}$ were considered. Therefore, a natural improvement to this scheme is to compute Eqs. (17) and (27) numerically and match the two at a point $r_{\text{match}}$ in the overlapping region, via

$$\left( R_{\text{near}} \frac{dR_{\text{far}}}{dr} - R_{\text{far}} \frac{dR_{\text{near}}}{dr} \right) \Bigg|_{r=r_{\text{match}}} = 0. \qquad (39)$$

Since Eqs. (17) and (27) are both approximate solutions, one should find nonzero residuals after plugging them into the original radial equation (5). The point $r_{\text{match}}$ is chosen such that relative residuals of the two solutions are equal or closest. This approach makes use of the analytic solutions, $R_{\text{far}}$ and $R_{\text{near}}$, but matches them numerically. Therefore, the method is semianalytic.

In Fig. 1, we perform a comparison of the growth rates calculated with different methods. We first consider the case of $\mathcal{K} = 0$, which corresponds to the purely ingoing boundary condition for a BH. In this case, other than the analytic method and the semianalytic method explained above, the growth rate $\omega_I$ can also be calculated using the continued fraction method [17], which serves as a consistency check here. For our choice of parameters, the analytic results agree very well with the continued fraction results in the regime $\alpha \ll 1$, but the discrepancy quickly increases for a larger $\alpha$. However, the semianalytic method always yields a result close to that of the continued fraction method for the full range of $\alpha$ considered, with a relative error less than 50%.

When $\mathcal{K} \neq 0$, the continued fraction method by Dolan [17] cannot be used, because the inner boundary condition is no longer purely ingoing. In this case, in order to relate the semianalytic results for ECOs to those for BHs, we also show a third curve in dashed purple in each of the last two
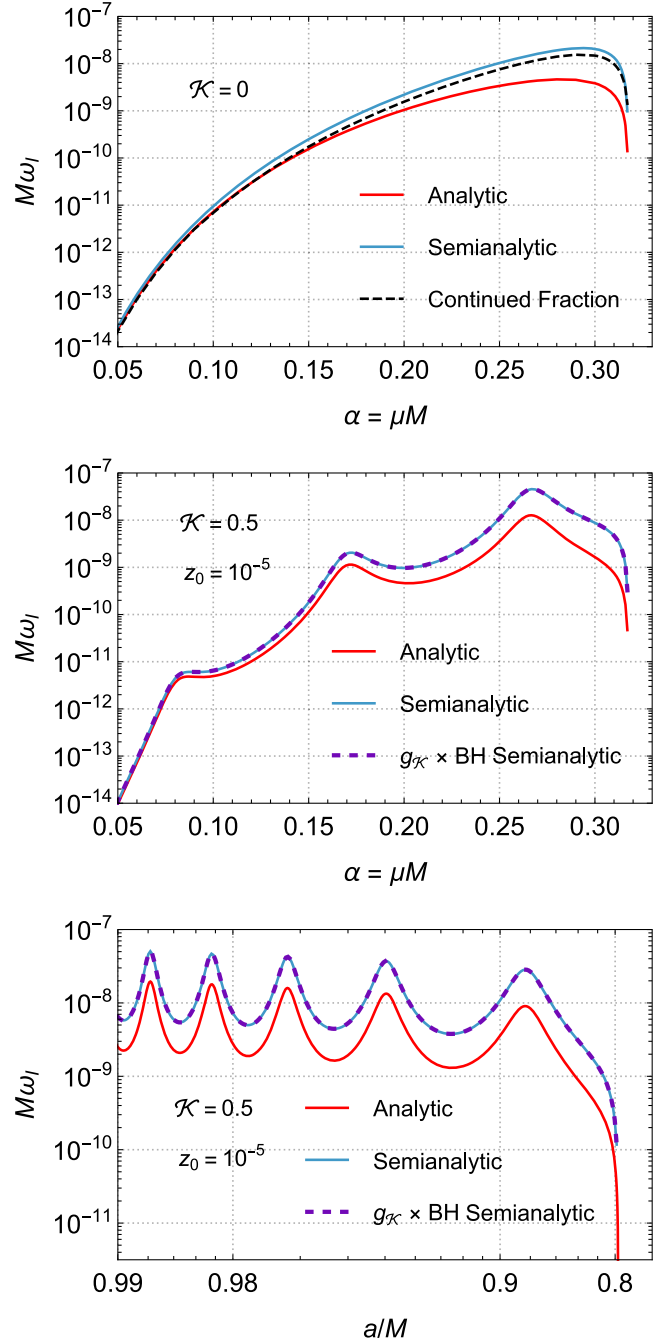


FIG. 1. Comparison of different methods in calculating the (dimensionless) superradiance growth rate $M\omega_I$. Growth rates $M\omega_I$ of the fundamental mode ($l = m = 1$ and $n = 0$), calculated using the analytic method and the semianalytic method, are shown for BHs (upper) and ECOs (middle and bottom), with $a/M = 0.9$ for the first two panels and $\mu M = 0.25$ for the last. For the BH case, we also present the result calculated using the continued fraction method for comparison. For the ECO cases, additionally, we multiply the semianalytic results for their corresponding BHs by $g_{\mathcal{K}}$, and plot the resulting growth rates with dashed purple curves.
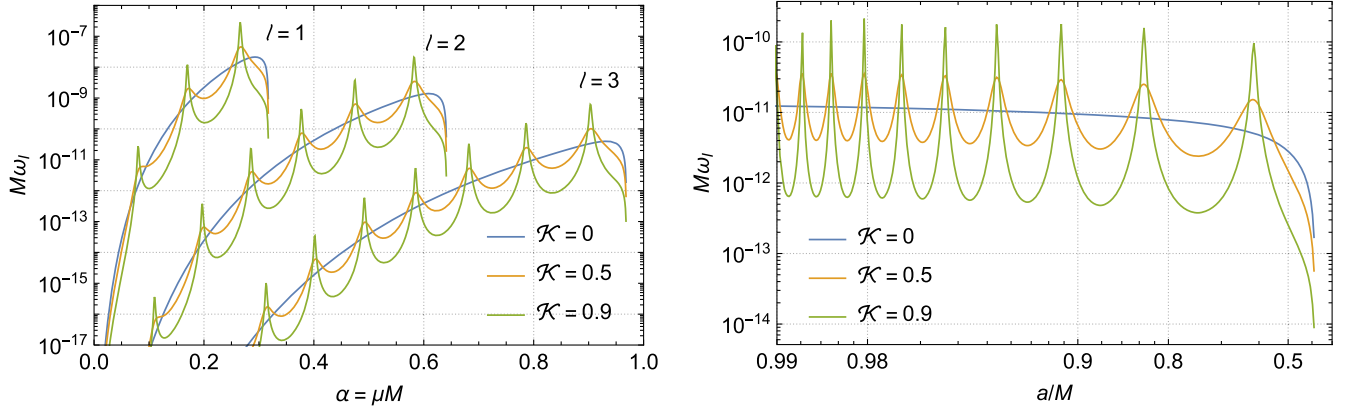
FIG. 2. Growth rate calculated using the semianalytic method, shown as functions of (left) the scalar mass parameter $\alpha$ and (right) the ECO's (dimensionless) spin $a/M$. The inner boundary is located at $z_0 = 10^{-5}$. For the left panel, we take $a/M = 0.9$ and plot the modes $(l, m, n) = (1, 1, 0)$, $(2, 2, 0)$, and $(3, 3, 0)$. For the right, we take $\mu M = 0.1$, and only the mode $(l, m, n) = (1, 1, 0)$ is shown.

panels of Fig. 1. This curve was obtained by multiplying the semianalytic results for BHs by $g_\mathcal{K}$. The striking point is, it perfectly agrees with the semianalytic results for ECOs, with a relative error less than $10^{-3}$. Therefore, even though the correction factor $g_\mathcal{K}$ was obtained using the fully analytical approach in the regime $\alpha \ll 1$, it turns out to also be applicable to the more accurate semianalytical results, which is not limited to that regime.

In the last two panels of Fig. 1, the growth rate exhibits oscillatory behaviors, introduced by the boundary reflection. In order to see how the value of the reflectivity changes these oscillating patterns, in Fig. 2, we present the growth rate for different $\mathcal{K}$, calculated using the semi-analytic method. It can be seen that for a larger $|\mathcal{K}|$, the curve shows sharper peaks with deeper valleys in between. These new features can affect the time evolution of superradiant instabilities and the ultralight particle mass constraints. These will be investigated in Secs. V and VI; but before that, we examine the physical origin of the correction factor $g_\mathcal{K}$ in the next section.

## IV. PHYSICAL INTERPRETATION OF $g_\mathcal{K}$

Here, we try to understand Eq. (35) and the correction factor $g_\mathcal{K}$ by analyzing the energy-momentum conservation at the ECO's surface $r = r_0$. A similar analysis for BHs can be found in Ref. [17].

A complex scalar field has a Lagrangian density $\mathcal{L} = \frac{1}{2}(\partial^\rho \Psi \partial_\rho \Psi^* + \mu^2 \Psi^* \Psi)$, and an energy-momentum tensor $T^{\mu\nu} = \partial^{(\mu}\Psi \partial^{\nu)}\Psi^* - g^{\mu\nu}\mathcal{L}$. Following Dolan [17], we use the ingoing-Kerr coordinates $\tilde{x}^\mu = (\tilde{t}, r, \theta, \tilde{\phi})$, defined via

$$\tilde{t} = t + \alpha(r), \qquad \tilde{\phi} = \phi + \beta(r), \qquad (40)$$

where

$$\alpha(r) = \frac{2M}{r_+ - r_-}(r_+ \ln|r - r_+| - r_- \ln|r - r_-|),$$

$$\beta(r) = \frac{a}{r_+ - r_-}\ln\left|\frac{r - r_+}{r - r_-}\right|. \qquad (41)$$

Hereafter, we add a tilde on top of quantities calculated in this coordinate system. The contravariant metric tensor is

$$\tilde{g}^{\mu\nu} = \frac{1}{\rho^2}\begin{pmatrix} -\rho^2 - 2Mr & 2Mr & 0 & 0 \\ 2Mr & \Delta & 0 & a \\ 0 & 0 & 1 & 0 \\ 0 & a & 0 & 1/\sin^2\theta \end{pmatrix}, \qquad (42)$$

where $\rho$ and $\Delta$ are the same as in Eq. (2). Note that our convention differs from that of Dolan [17] by a minus sign. In this case, the Klein-Gordon equation is separable using

$$\tilde{\Psi}(\tilde{t}, r, \theta, \tilde{\phi}) = e^{-i\omega\tilde{t}}e^{im\tilde{\phi}}S_{lm}(\theta)\tilde{R}_{lm}(r). \qquad (43)$$

The spacetime has a Killing vector $\partial_{\tilde{t}}$, and $\tilde{T}_0{}^\mu$ is the conserved energy flux. We consider the spacetime region $V$ that describes a time slice of the external space, satisfying $-\Delta\tilde{t}/2 < \tilde{t} < \Delta\tilde{t}/2$, $r > r_0$, $0 \leq \theta < \pi$, and $0 \leq \tilde{\phi} < 2\pi$. Then the conservation law, $\nabla_\mu \tilde{T}_0{}^\mu = 0$, together with Gauss's theorem, gives

$$\int_{\partial V} \tilde{T}_0{}^\mu \tilde{n}_\mu \sqrt{|\tilde{g}|}\,d^3\tilde{S} = 0, \qquad (44)$$

where $\tilde{g} \equiv -\rho^4 \sin^2\theta$ is the determinant of the covariant metric $\tilde{g}_{\mu\nu}$, and $\tilde{n}_\nu$ is the normal one-form of $\partial V$. Here, $\tilde{n}_\nu = \pm\delta_\nu^0$ for the hypersurfaces $\tilde{t} = \pm\Delta\tilde{t}/2$, and $\tilde{n}_\nu = \delta_\nu^1$ for the hypersurface $r = r_0$. The hypersurface at spatial infinity $r \to \infty$ is not included because the energy flux is zero there. When $\Delta\tilde{t} \to 0$, Eq. (44) yields the energy conservation equation,
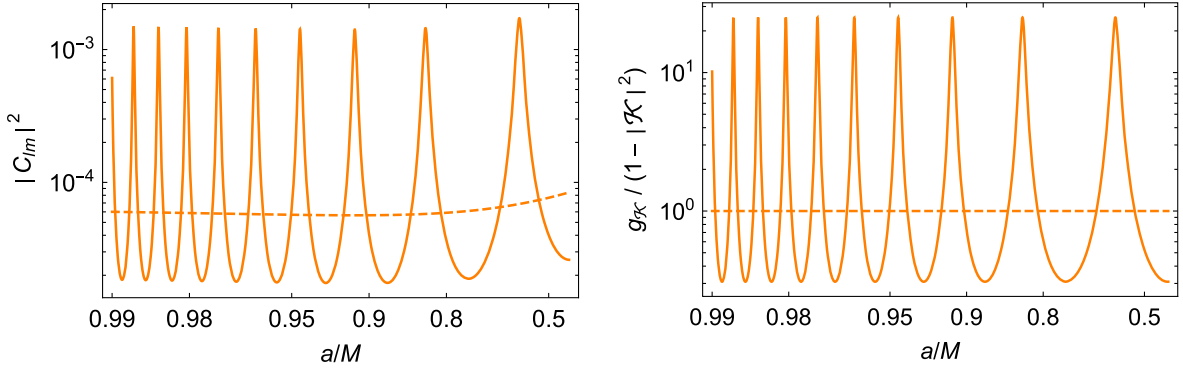
FIG. 3. A comparison between $|C_{lm}|^2$ and $g_{\mathcal{K}}/(1 - |\mathcal{K}|^2)$. Solid lines are for an ECO with $\mathcal{K} = 0.8$ and $z_0 = 10^{-5}$, while dashed lines are their counterparts for a BH ($\mathcal{K} = 0$). We take $\mu M = 0.1$ and consider the fundamental mode $l = m = 1$ and $n = 0$. The relative amplitude $C_{lm}$ is calculated using the analytic method.

$$\frac{\partial}{\partial \tilde{t}} \int_{3D} -\tilde{T}_0^{\,0} \rho^2 \sin\theta \, dr \, d\theta \, d\tilde{\phi} = \int_{2D} -\tilde{T}_0^{\,1} \rho^2 \sin\theta \, d\theta \, d\tilde{\phi}, \tag{45}$$

where the "3D" integration is done in the external space $(r > r_0)$, and the "2D" integration on the surface $r = r_0$, both at the fixed time $\tilde{t} = 0$.

In order to obtain the asymptotic behavior of $\tilde{R}_{lm}$, we compare Eqs. (4) and (43), and find that the radial function in the ingoing-Kerr coordinates $\tilde{R}_{lm}$ and that in the Boyer-Lindquist coordinates $R_{lm}$ are related by

$$\tilde{R}_{lm}(r) = e^{i\omega\alpha(r)} e^{-im\beta(r)} R_{lm}(r). \tag{46}$$

Therefore, when $r \to r_0$, the radial function $\tilde{R}_{lm}$ behaves as

$$\tilde{R}_{lm} \sim z^{ip} R_{lm} \sim z^{ip} \cdot C_{lm}[(z/z_0)^{-ip} + \mathcal{K}(z/z_0)^{ip}], \tag{47}$$

where $C_{lm}$ is a constant. Since in our calculation, from Eq. (17) to the subsequent matching procedure, the absolute magnitude of the field is not specified, we call $C_{lm}$ the "relative amplitude" of the field at the inner boundary.[5] In most cases, $|C_{lm}|^2 \ll 1$. Using the transformed wave function $\tilde{\Psi}$ (43) and the asymptotic behavior of $\tilde{R}_{lm}$ (47), direct calculation yields

$$-\tilde{T}_0^{\,1} = \frac{\omega_R(ma - 2Mr_+\omega_R)}{\rho_0^2} |C_{lm}|^2 (1 - |\mathcal{K}|^2) |S(\theta)|^2, \tag{48}$$

which is the net energy flux going outwards at $r_0$, defined in the ingoing-Kerr coordinates. Calculating the 2D integral in Eq. (45), we obtain

$$2\omega_I = \omega_R(1 - |\mathcal{K}|^2) \frac{(ma - 2Mr_+\omega_R)|C_{lm}|^2}{\int_{3D} -\tilde{T}_0^{\,0} \rho^2 \sin\theta \, dr \, d\theta \, d\tilde{\phi}}, \tag{49}$$

where the $2\omega_I$ term arises because $\tilde{T}_0^{\,0} \propto e^{2\omega_I \tilde{t}}$. The integral in the denominator represents the total energy outside $r_0$. As long as $|C_{lm}|^2 \ll 1$, the integral mainly depends on the far region solution $R_{\text{far}}(r)$ and therefore, can be approximately evaluated using a hydrogenic wave function in a Newtonian potential. As a result, this integral has a very weak dependence on $a/M, z_0$, and $\mathcal{K}$, and mainly depends on $l$ and $n$.

Equations (48) and (49) provide a way to understand the physical meaning of $g_{\mathcal{K}}$ in Eq. (36). First, let us consider the overall suppression factor $(1 - |\mathcal{K}|^2)$. This factor also appears in Eq. (48), and its interpretation is straightforward: the energy flows carried by the ingoing and outgoing waves go on opposite directions, and thus, the net flux is reduced when there is a (partially) reflecting surface. In particular, when $|\mathcal{K}| = 1$, the two achieve a balance, and thus, there is no net energy flux across $r_0$, leading to a zero growth/decay rate.[6]

The denominator of $g_{\mathcal{K}}$, which represents the oscillatory behavior of $\omega_I$, is tightly related to the relative amplitude $C_{lm}$. To demonstrate this, in the left panel of Fig. 3, we plot $|C_{lm}|^2$ for $\mathcal{K} = 0.8$ (solid) and $\mathcal{K} = 0$ (dashed). For classical BHs, $|C_{lm}|^2$ changes very slowly with $a$. However, in the presence of a boundary reflection, the change becomes rapid. The oscillatory behavior of $|C_{lm}|^2$ directly leads to the oscillatory behavior of $\omega_I$ via Eq. (49), manifested as the oscillating denominator of $g_{\mathcal{K}}$, as shown in the right panel of Fig. 3. The physical link between the relative amplitude and the growth rate is also

---

[5]Strictly speaking, the value of the radial function $R_{lm}$ at $r = r_0$ is $C_{lm}(1 + \mathcal{K})$.

[6]Since the denominator in Eq. (36) ranges from $(1 - |\mathcal{K}|)^2$ to $(1 + |\mathcal{K}|)^2$, one may wonder what if $|\mathcal{K}| = 1$ and both the numerator and denominator are equal to zero. In this case, $g_{\mathcal{K}} \to \infty$. However, once the spin $a$ decreases due to extraction of the angular momentum, the denominator would be nonzero, and $g_{\mathcal{K}}$ stays at 0 thereafter.

straightforward: with a larger $|C_{lm}|^2$, the scalar field extracts a larger energy flux (48) and thus, grows faster.

To sum up, in the analytical expression of $g_{\mathcal{K}}$ (36), the factor $(1 - |\mathcal{K}|)^2$ can be understood as the counteraction of outgoing and ingoing energy flows, and the oscillatory behavior of the denominator comes from the change in the scalar field's (relative) density $|C_{lm}|^2$ at $r = r_0$, which is proportional to the amount of energy extracted there.

## V. TIME EVOLUTION OF SUPERRADIANT INSTABILITY

In this section, we consider the time evolution of superradiant instabilities and investigate how it is influenced by the boundary reflection.

Let us start by reviewing the case of a Kerr BH. If initially there is a nonzero scalar field around a Kerr BH (for example, arising from quantum fluctuations), as long as the superradiance condition (1) is satisfied, the field will extract energy and angular momentum from the BH. In this case, more and more scalar particles are produced, the field grows exponentially, and a bosonic cloud around the BH is formed. For scalar fields, the time evolution of superradiant instabilities around Kerr BHs has been investigated using an adiabatic approximation in Ref. [26]. For the case of an ECO, the superradiance condition is not changed. Similar to its BH counterpart, a scalar field could grow and form a bosonic cloud when the superradiance condition is satisfied. However, since the growth rate is changed by the factor $g_{\mathcal{K}}$, one will anticipate some new features in the time evolution.

To begin with, we present the equations governing the adiabatic evolution of the instability. These equations are essentially the same as in the case of a Kerr BH. First, since the wave function $\Psi$ grows as $\sim e^{\omega_I t}$, the number of particles in the bosonic cloud grows as $\sim e^{2\omega_I t}$. Therefore, the superradiant energy extraction rate is

$$\dot{E}_{\mathrm{SR}} = 2\omega_I M_{\mathrm{cl}}, \qquad (50)$$

where $M_{\mathrm{cl}}$ is the mass of the bosonic could. Since we are mostly interested in the case where gas accretion is much slower than the evolution of superradiant instabilities, we will not take possible accretion processes onto the central ECO into account.[7] Then, the mass $M$ and angular momentum $J$ of the ECO change according to

$$\dot{M} = -\dot{E}_{\mathrm{SR}}, \qquad (51)$$

$$\dot{J} = -\frac{m}{\omega_R}\dot{E}_{\mathrm{SR}}. \qquad (52)$$

---

[7]See Ref. [26], where gas accretion is included in the evolution equations for BHs.

On the other hand, the mass of the bosonic cloud changes as

$$\dot{M}_{\mathrm{cl}} = \dot{E}_{\mathrm{SR}} - \dot{E}_{\mathrm{GW}}, \qquad (53)$$

where $\dot{E}_{\mathrm{GW}}$ is the energy flux carried away by GWs emitted by the cloud. In our study below, we only consider the fundamental mode, $l = m = 1$ and $n = 0$, for which we can adopt the GW energy flux obtained in Ref. [26],

$$\dot{E}_{\mathrm{GW}} = \frac{484 + 9\pi^2}{23040}\left(\frac{M_{\mathrm{cl}}^2}{M^2}\right)(M\mu)^{14}. \qquad (54)$$

This equation, obtained for the case of BHs, is supposed to be a good approximation still for the case of ECOs. The reason is that the GW emission mostly comes from the far region where $|\Psi|^2$ is large, and the far region wave functions in both the BH and the ECO cases are nearly the same.

Using the parameters listed in Table I, we can calculate the time evolution of superradiant instabilities. Here, the initial mass of the bosonic cloud is taken to be the mass of a particle, $M_{\mathrm{cl},0} = \mu$. The results are plotted in Fig. 4 for different values of reflectivity and scalar particle mass. We found that the evolution can be roughly divided into three stages.

*Steady growth of the scalar field* In the very beginning, the mass of the cloud is so small (in fact for $\mu = 1 \times 10^{-18}$ eV and $M_0 = 10^7 M_\odot$, we have $M_{\mathrm{cl},0}/M_0 \sim 10^{-91}$) that the superradiant extraction is negligible. Therefore, the mass and spin of the ECO are essentially unchanged for a long period, and consequently, the growth rate $\omega_I$ stays steady.

*A spin-down phase of the ECO* After about 200 e-folds, the cloud has acquired a non-negligible mass $\sim 10^{-5} M_0$, and the evolution starts to be discernible in the figure. The cloud quickly extracts energy and angular momentum from the ECO, until it reaches the maximal mass $\sim 0.1 M_0$. This stage lasts for about ten e-folds, during which the spin of the ECO drops quickly. Therefore, as implied in the right panel of Fig. 2, the growth rate $\omega_I$ shows an oscillatory pattern

TABLE I. Definition of parameters for the time evolution of superradiant instabilities.

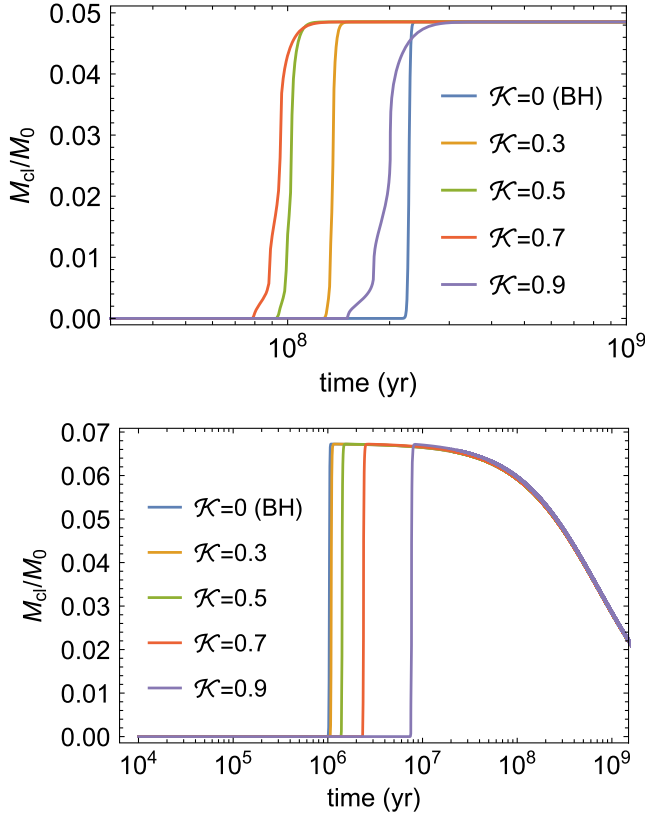| Parameter | Definition |
|---|---|
| $M_0$ | Initial mass of the ECO |
| $M_{\mathrm{cl},0}$ | Initial mass of the bosonic cloud |
| $J_0$ | Initial spin of the ECO |
| $\mu$ | Mass of the ultralight scalar particle |
| $z_0$ | Location of the reflective boundary in Eq. (21) |
| $\mathcal{K}$ | Reflectivity of the boundary surface |

FIG. 4. Time evolution of the mass of the bosonic cloud. We take $M_0 = 10^7 M_\odot$, $J_0/M_0^2 = 0.9$, $z_0 = 10^{-5}$, and only consider the fundamental mode with $l = m = 1$ and $n = 0$. We have used $\mu = 1 \times 10^{-18}$ eV and $2 \times 10^{-18}$ eV for the upper and lower panels, respectively, corresponding to $\mu M = 0.075$ and $\mu M = 0.15$.

with time. As an obvious example, the growth for the $\mathcal{K} = 0.9$ case in the upper panel of Fig. 4 is uneven during this stage.

*GW dissipation* After the spin of the ECO drops to the superradiant critical value, GW emission overtakes the superradiant extraction, and therefore, the cloud starts to dissipate gradually. GWs emitted by the cloud are nearly monochromatic with an angular frequency $\sim 2\omega_R$ and a slowly decreasing amplitude [33,36,38].

In Fig. 4, we can see that for different $\mathcal{K}$, the time the cloud takes to accumulate to its maximal mass can vary. This timescale is mainly determined by the first stage, during which the growth rate $\omega_I$ is essentially a constant. The boundary reflection changes this timescale via the correction factor $g_\mathcal{K}$ in $\omega_I$. Since $g_\mathcal{K}$ can be either larger or less than 1, this timescale, compared to the BH case, can be either shortened or prolonged by the boundary reflection, as seen in the upper (shortened) and lower (prolonged) panels of Fig. 4, respectively. The change in the growth timescale implies that the boundary reflection may affect constraints on the ultralight particle mass, which is the topic of the next section.

## VI. ASTROPHYSICAL CONSTRAINTS ON THE MASS OF ULTRALIGHT BOSONS

In this section, we first review how superradiant instabilities can be used to constrain the mass of ultralight bosons, and then discuss the implications of the reflective boundary condition if the assumed BH is in fact an ECO.

### A. Ultralight particle mass constraints from BHs

Constraints on the mass of ultralight bosons have been imposed considering BH superradiance, with measurements of BHs' spin and mass [5,33,39,40]. The basic idea is that, if there exists an ultralight particle with mass $\mu$, BHs with high enough spins should suffer superradiant instabilities and spin down. This results in an exclusion region on the $J - M$ plane (Regge plane), where $J$ and $M$ are respectively the angular momentum and mass of BHs. The location of this region is related to the mass of the particle $\mu$. Therefore, values of $\mu$ which create exclusion regions that are incompatible with existing BH $J - M$ measurements should not be allowed.

To estimate the exclusion regions, one approach is to compare the characteristic timescale of the bosonic cloud evolution, $\tau_{\text{cloud}}$, with the characteristic timescale associated to the BH's astrophysical processes, $\tau_{\text{astro}}$. For example, for the case of binary BHs, Arvanitaki *et al.* [40] compared the superradiance saturation timescale, namely the time the cloud takes to accumulate to its maximal mass, with the binary merger timescale. For the case of x-ray binaries, Cardoso *et al.* [39] compared the instability timescale, $1/\omega_I$, with the durations over which two sources show stable spin values. The typical astrophysical timescale is also often chosen to be the accretion timescale of the BH [5,18,34,67]. If $\tau_{\text{cloud}} \ll \tau_{\text{astro}}$, the cloud could extract energy and angular momentum effectively within an astrophysical timescale, substantially spinning down the BH. Another approach to find the exclusion regions is the Monte Carlo method [26]. Starting with a particular $(J, M)$ combination, one can calculate the evolution of the system and extract the final state of the BH at some specified time $t_F$. Doing this for a sample of randomly chosen initial states, $(J_i, M_i)$, and plotting the final states, $(J_f, M_f)$, on the Regge plane, one can find that a particular region is hardly populated; see Fig. 3 in Ref. [26] for example.

### B. Extension to the ECO case and the role of boundary reflection

Previous mass constraints of ultralight particles were obtained based on the assumption that the compact objects are BHs, with an event horizon as the inner boundary. However, it is worth studying how the change in the boundary condition affects the mass constraints. Here, we make a brief discussion on how the ECO boundary condition alters the $J - M$ exclusion regions, as well as its implications for ultralight particle mass constraints.

For simplicity, we adopt the first approach, i.e., comparing timescales, to draw exclusion regions on the Regge plane. Here, the astrophysical timescale is taken to be the accretion timescale, $\tau_{\mathrm{Acc}}$, of the ECO. We assume that the ECO is accreting at a rate $f_{\mathrm{Edd}}\dot{M}_{\mathrm{Edd}}$, where $\dot{M}_{\mathrm{Edd}}$ is the Eddington accretion rate, which is related to the Eddington luminosity $L_{\mathrm{Edd}}$ through the radiative efficiency $\eta$, via $\epsilon\dot{M}_{\mathrm{Edd}}c^2 = L_{\mathrm{Edd}} = 1.26 \times 10^{31}(M/M_\odot)\,\mathrm{J\,s^{-1}}$. The factor $\epsilon \equiv \eta/(1 - \eta)$ arises because if a fraction $\eta$ of the infalling mass is converted to radiation, the accreted fraction reduces to $1 - \eta$. Here, we define the accretion timescale,

$$\tau_{\mathrm{Acc}} \equiv \frac{M}{f_{\mathrm{Edd}}\dot{M}_{\mathrm{Edd}}} = \frac{4.5 \times 10^7}{f_{\mathrm{Edd}}}\frac{\epsilon}{0.1}\mathrm{yr}, \qquad (55)$$

where we shall typically take $\epsilon = 0.1$ [68,69].

If we consider a supermassive ECO with mass $M \sim 10^6 M_\odot$ and take the initial mass of the cloud to be the mass of a single scalar particle $\mu \sim 10^{-18}$ eV, it takes the cloud about $\ln(0.1M/\mu) \sim 205$ $e$-folds to grow to $0.1M$. Therefore, we define the fast-superradiance regime satisfying

$$205 \ln\left(\frac{M}{10^6 M_\odot}\frac{10^{-18}\,\mathrm{eV}}{\mu}\right)\tau_{\mathrm{SR}} < \tau_{\mathrm{Acc}}, \qquad (56)$$

where the superradiance $e$-fold timescale is $\tau_{\mathrm{SR}} \equiv 1/(2\omega_I)$ since the cloud grows as $M_{\mathrm{cl}} \propto e^{2\omega_I t}$. In this regime, the cloud will extract energy and angular momentum effectively within the accretion timescale. Therefore, it gives an exclusion region on the Regge plane. BHs ($\mathcal{K} = 0$) or ECOs ($\mathcal{K} \neq 0$) inside this region should spin down effectively and leave this region within $\tau_{\mathrm{Acc}}$.

We calculated the growth rate $\omega_I$ using the analytic method. Exclusion regions defined in Eq. (56) are plotted in Fig. 5 for different values of the boundary reflectivity $\mathcal{K}$. It is clear that the boundary reflection alters the shape of this region and introduces small spiky features, which are more pronounced as $|\mathcal{K}|$ increases. When $\mathcal{K}$ approaches extremity $|\mathcal{K}| \to 1$, the spikes are sharper, while the bulk part—the part under the spikes, as illustrated in the figure for $\mathcal{K} = 0.99$—shrinks inwards.

Our results may have some implications for the usual method for constraining the scalar mass. When the reflectivity is not too large, the alteration to the exclusion region is insignificant. For example, in the $\mathcal{K} = 0.5$ case of Fig. 5, compared with the $\mathcal{K} = 0$ case, for every value of $J/M^2$, the change in the value of $M$ on the boundary line is within 0.1 dex, which can be comparable to, say, the current measurement errors. However, for $\mathcal{K} = 0.99$, the spikes are distinct, and the shrinkage of the bulk region reaches $\sim 0.4$ dex. Therefore, we expect that a mildly reflective boundary, roughly $|\mathcal{K}| \lesssim 0.5$, may not substantially influence the mass constraints of ultralight scalar particles, but an extreme value of reflectivity, say, $|\mathcal{K}| \gtrsim 0.9$, could
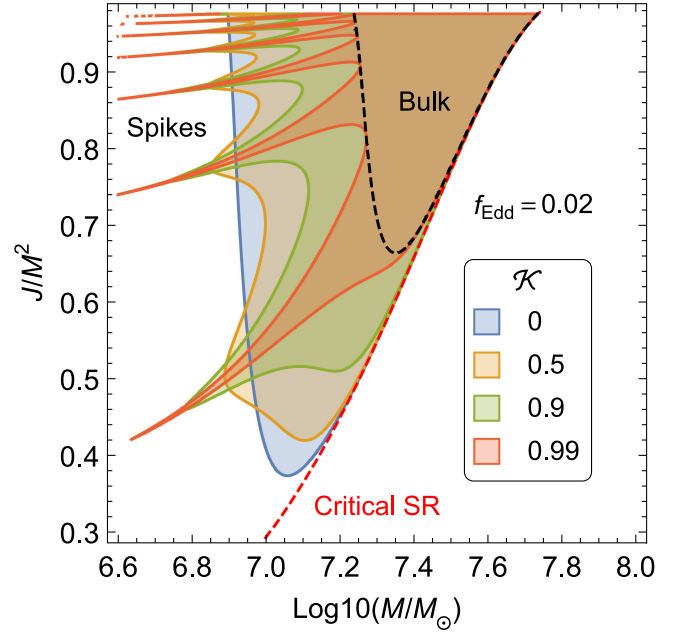


FIG. 5. Exclusion regions, as defined in Eq. (56), for different $\mathcal{K}$. The red dashed line denotes where the superradiance condition (1) is saturated. The vertical axis extends up to $J/M^2 = 0.975$, above which the small spikes are much more crowded. We have taken $z_0 = 10^{-5}$ and $\mu = 10^{-18}$ eV.

introduce distinct spiky structures to the exclusion region, with a considerable inward shrinkage of its bulk part.

## VII. CONCLUSION

Exotic compact objects (ECOs) have been conceived as alternatives to BHs. ECOs do not possess an event horizon, and the inner boundary condition for scalar perturbations is different from that of BHs. In this paper, we computed the growth rate of superradiant instabilities assuming a modified inner boundary condition, parametrized by the location of a reflective surface, $z_0$, and its reflectivity, $\mathcal{K}$. We solved the eigenvalue problem analytically, using matched asymptotic expansions, and found the analytic expression of the growth rate $\omega_I$. Our key result is that the growth rate of superradiant instabilities around an ECO can be related to the value in the BH case simply by a factor $g_{\mathcal{K}}$, whose explicit expression is given in Eq. (36). For a better accuracy, we also calculated the growth rate using a semianalytic method. We found that the semianalytic results in the ECO and BH cases can also be related by the same factor $g_{\mathcal{K}}$, despite the fact that this factor was obtained using a purely analytic treatment. Therefore, the factor $g_{\mathcal{K}}$ must have a clear physical meaning, which was investigated, and we showed that it can be related to the energy flux at the inner boundary.

Using an adiabatic approach, we also studied how the superradiant instability of such ECOs would evolve. We found that, starting from a single particle, the evolution can

be divided into three stages, namely (i) steady growth of the scalar field, (ii) a spin-down phase of the ECO, and (iii) GW dissipation. The time it takes for the cloud to reach its maximal mass mainly depends on the duration of the first stage and can be either shortened or prolonged by the boundary reflection.

Finally, we discussed the implications for astrophysical constraints on ultralight scalar fields. By comparing the timescales of the cloud evolution and gas accretion, we found the exclusion regions on the ECOs' Regge plane. Boundary reflection introduces spiky structures to the exclusion region, and the effect is more pronounced for larger reflectivities. As long as the reflectivity is not too large, say $|\mathcal{K}| \lesssim 0.5$, the alteration to the exclusion region may not substantially influence the mass constraints of ultralight scalars, but the effects of boundary reflection could be significant for large reflectivity, e.g., $|\mathcal{K}| \gtrsim 0.9$.

At the end of this paper, we make a short comment on the ECO model we adopted. Our work is based on the model in which one truncates the Kerr spacetime at a radius $r_0$ and puts a spherical reflective boundary there with an isotropic reflectivity $\mathcal{K}$. Although widely used in literature (as mentioned in the Introduction and references therein), this model is only a simplified one. More realistic models may consider deviation of the boundary shape from a sphere and also anisotropic reflectivity, which is out of the scope of this work and deserves future study.

## ACKNOWLEDGMENTS

## APPENDIX: DETERMINING THE RATIO $b_4/b_3$

When $z \to 0$, we have

$$\left(\frac{z}{1+z}\right)^{-ip} u_3 \to f_3^- z^{-ip} + f_3^+ z^{ip}, \tag{A1}$$

$$\left(\frac{z}{1+z}\right)^{-ip} u_4 \to f_4^- z^{-ip} + f_4^+ z^{ip}, \tag{A2}$$

where

$$f_3^- = \frac{(-1)^{l'}\Gamma(-2l')\Gamma(2ip)}{\Gamma(-l')\Gamma(2ip - l')}, \tag{A3}$$

$$f_3^+ = \frac{(-1)^{l'}\Gamma(-2l')\Gamma(-2ip)}{\Gamma(-l')\Gamma(-l' - 2ip)}, \tag{A4}$$

$$f_4^- = \frac{(-1)^{1-l'}\Gamma(2l' + 2)\Gamma(2ip)}{\Gamma(l' + 1)\Gamma(l' + 2ip + 1)}, \tag{A5}$$

$$f_4^+ = \frac{(-1)^{1-l'}\Gamma(2l' + 2)\Gamma(-2ip)}{\Gamma(l' + 1)\Gamma(l' - 2ip + 1)}. \tag{A6}$$

The inner boundary condition (14) is equivalent to

$$\lim_{z \to z_0} R_{\text{near}} \sim (z/z_0)^{-ip} + \mathcal{K}(z/z_0)^{ip}. \tag{A7}$$

Considering the boundary condition and the asymptotic behaviors of $u_3$, $u_4$, we can pin down the ratio $b_4/b_3$ via

$$\frac{b_3 f_3^+ + b_4 f_4^+}{b_3 f_3^- + b_4 f_4^-} = \mathcal{K} z_0^{-2ip}, \tag{A8}$$

and the result is presented in Eq. (28) in the main text.

[1] R. D. Peccei and H. R. Quinn, Phys. Rev. Lett. **38**, 1440 (1977).
[2] S. Weinberg, Phys. Rev. Lett. **40**, 223 (1978).
[3] F. Wilczek, Phys. Rev. Lett. **40**, 279 (1978).
[4] A. Arvanitaki, S. Dimopoulos, S. Dubovsky, N. Kaloper, and J. March-Russell, Phys. Rev. D **81**, 123530 (2010).
[5] A. Arvanitaki and S. Dubovsky, Phys. Rev. D **83**, 044026 (2011).
[6] M. Goodsell, J. Jaeckel, J. Redondo, and A. Ringwald, J. High Energy Phys. 11 (2009) 027.
[7] B. Li, T. Rindler-Daller, and P. R. Shapiro, Phys. Rev. D **89**, 083536 (2014).
[8] L. Hui, J. P. Ostriker, S. Tremaine, and E. Witten, Phys. Rev. D **95**, 043541 (2017).
[9] D. Antypas et al., arXiv:2203.14915.
[10] Z. Wang and L. Shao, Phys. Rev. D **103**, 116021 (2021).

[11] R. Brito, V. Cardoso, and P. Pani, Lect. Notes Phys. **906**, 1 (2015).

[12] T. J. Zouros and D. M. Eardley, Ann. Phys. (N.Y.) **118**, 139 (1979).

[13] S. Detweiler, Phys. Rev. D **22**, 2323 (1980).

[14] H. Furuhashi and Y. Nambu, Prog. Theor. Phys. **112**, 983 (2004).

[15] V. Cardoso, O. J. C. Dias, J. P. S. Lemos, and S. Yoshida, Phys. Rev. D **70**, 044039 (2004); **70**, 049903(E) (2004).

[16] V. Cardoso and S. Yoshida, J. High Energy Phys. 07 (2005) 009.

[17] S. R. Dolan, Phys. Rev. D **76**, 084001 (2007).

[18] P. Pani, V. Cardoso, L. Gualtieri, E. Berti, and A. Ishibashi, Phys. Rev. D **86**, 104017 (2012).

[19] R. Brito, V. Cardoso, and P. Pani, Phys. Rev. D **88**, 023514 (2013).

[20] S. R. Dolan, Phys. Rev. D **98**, 104006 (2018).

[21] D. Baumann, H. S. Chia, J. Stout, and L. ter Haar, J. Cosmol. Astropart. Phys. 12 (2019) 006.

[22] S.-S. Bao, Q.-X. Xu, and H. Zhang, Phys. Rev. D **106**, 064016 (2022).

[23] O. J. C. Dias, G. Lingetti, P. Pani, and J. E. Santos, Phys. Rev. D **108**, L041502 (2023).

[24] S. R. Dolan, Phys. Rev. D **87**, 124026 (2013).

[25] H. Witek, V. Cardoso, A. Ishibashi, and U. Sperhake, Phys. Rev. D **87**, 043513 (2013).

[26] R. Brito, V. Cardoso, and P. Pani, Classical Quantum Gravity **32**, 134001 (2015).

[27] W. E. East, Phys. Rev. Lett. **121**, 131104 (2018).

[28] H. Yoshino and H. Kodama, Prog. Theor. Phys. **128**, 153 (2012).

[29] H. Yoshino and H. Kodama, Classical Quantum Gravity **32**, 214001 (2015).

[30] M. Baryakhtar, M. Galanis, R. Lasenby, and O. Simon, Phys. Rev. D **103**, 095019 (2021).

[31] H. Omiya, T. Takahashi, T. Tanaka, and H. Yoshino, J. Cosmol. Astropart. Phys. 06 (2023) 016.

[32] H. Yoshino and H. Kodama, Prog. Theor. Exp. Phys. **2014**, 043E02 (2014).

[33] A. Arvanitaki, M. Baryakhtar, and X. Huang, Phys. Rev. D **91**, 084011 (2015).

[34] M. Baryakhtar, R. Lasenby, and M. Teo, Phys. Rev. D **96**, 035019 (2017).

[35] R. Brito, S. Ghosh, E. Barausse, E. Berti, V. Cardoso, I. Dvorkin, A. Klein, and P. Pani, Phys. Rev. Lett. **119**, 131101 (2017).

[36] R. Brito, S. Ghosh, E. Barausse, E. Berti, V. Cardoso, I. Dvorkin, A. Klein, and P. Pani, Phys. Rev. D **96**, 064050 (2017).

[37] N. Siemonsen and W. E. East, Phys. Rev. D **101**, 024019 (2020).

[38] N. Siemonsen, T. May, and W. E. East, Phys. Rev. D **107**, 104003 (2023).

[39] V. Cardoso, Óscar J. C. Dias, G. S. Hartnett, M. Middleton, P. Pani, and J. E. Santos, J. Cosmol. Astropart. Phys. 03 (2018) 043.

[40] A. Arvanitaki, M. Baryakhtar, S. Dimopoulos, S. Dubovsky, and R. Lasenby, Phys. Rev. D **95**, 043001 (2017).

[41] V. Cardoso and P. Pani, Living Rev. Relativity **22**, 4 (2019).

[42] S. W. Hawking, Phys. Rev. D **14**, 2460 (1976).

[43] D. Marolf, Rep. Prog. Phys. **80**, 092001 (2017).

[44] S. D. Mathur, Fortschr. Phys. **53**, 793 (2005).

[45] K. Skenderis and M. Taylor, Phys. Rep. **467**, 117 (2008).

[46] L. Visinelli, Int. J. Mod. Phys. D **30**, 2130006 (2021).

[47] P. O. Mazur and E. Mottola, Universe **9**, 88 (2023).

[48] M. Visser, *Lorentzian Wormholes: From Einstein to Hawking* (American Institute of Physics, Melville, NY, 1995).

[49] T. Damour and S. N. Solodukhin, Phys. Rev. D **76**, 024016 (2007).

[50] V. Cardoso and P. Pani, Nat. Astron. **1**, 586 (2017).

[51] V. Cardoso, E. Franzin, and P. Pani, Phys. Rev. Lett. **116**, 171101 (2016); **117**, 089902(E) (2016).

[52] V. Cardoso, P. Pani, M. Cadoni, and M. Cavaglià, Phys. Rev. D **77**, 124044 (2008).

[53] C. F. B. Macedo, T. Stratton, S. Dolan, and L. C. B. Crispino, Phys. Rev. D **98**, 104034 (2018).

[54] E. Maggio, P. Pani, and V. Ferrari, Phys. Rev. D **96**, 104047 (2017).

[55] E. Maggio, V. Cardoso, S. R. Dolan, and P. Pani, Phys. Rev. D **99**, 064007 (2019).

[56] J. L. Friedman, Commun. Math. Phys. **62**, 247 (1978).

[57] G. Moschidis, Commun. Math. Phys. **358**, 437 (2018).

[58] Z. Mark, A. Zimmerman, S. M. Du, and Y. Chen, Phys. Rev. D **96**, 084002 (2017).

[59] C. P. Burgess, R. Plestid, and M. Rummel, J. High Energy Phys. 09 (2018) 113.

[60] E. Maggio, P. Pani, and G. Raposo, Testing the nature of dark compact objects with gravitational waves, in *Handbook of Gravitational Wave Astronomy*, edited by C. Bambi, S. Katsanevas, and K. D. Kokkotas (Springer Singapore, Singapore, 2020), pp. 1–37.

[61] R.-Z. Guo, C. Yuan, and Q.-G. Huang, Phys. Rev. D **105**, 064029 (2022).

[62] R.-Z. Guo, C. Yuan, and Q.-G. Huang, J. Cosmol. Astropart. Phys. 04 (2023) 069.

[63] E. Berti, V. Cardoso, and M. Casals, Phys. Rev. D **73**, 024013 (2006); **73**, 109902(E) (2006).

[64] E. Maggio, A. Testa, S. Bhagwat, and P. Pani, Phys. Rev. D **100**, 064056 (2019).

[65] H. Bateman, *Higher Transcendental Functions [Volumes I-III]* (McGraw-Hill Book Company, New York, 1953), Vol. 1.

[66] J. G. Rosa, J. High Energy Phys. 06 (2010) 015.

[67] P. Pani, V. Cardoso, L. Gualtieri, E. Berti, and A. Ishibashi, Phys. Rev. Lett. **109**, 131102 (2012).

[68] E. E. Salpeter, Astrophys. J. **140**, 796 (1964).

[69] F. Shankar, D. H. Weinberg, and J. Miralda-Escudé, Astrophys. J. **690**, 20 (2008).